LaNi<sub>x</sub>Fe<sub>1-x</sub>O<sub>3</sub> as flexible oxygen or carbon carriers for tunable syngas production and CO<sub>2</sub> utilization

Sherafghan Iftikhar<sup>1</sup>, William Martin<sup>1</sup>, Yunfei Gao<sup>1,2</sup>, Xinbin Yu<sup>3</sup>, Iwei Wang<sup>1</sup>, Zili Wu<sup>3</sup>, and Fanxing Li<sup>1</sup>\*

<sup>1</sup> Department of Chemical and Biomolecular Engineering, North Carolina State University, Raleigh, NC 27695-7905, United States

<sup>2</sup>Key Laboratory of Coal Gasification and Energy Chemical Engineering of Ministry of Education, Shanghai Engineering Research Center of Coal Gasification, East China University of Science and Technology, Shanghai 200237, PR China

<sup>3</sup>Oak Ridge National Laboratory, Chemical Science Division and Center for Nanophase Materials Sciences, Oak Ridge, TN, USA

\*fli5@ncsu.edu

#### **Abstract**

The current study reports LaFe<sub>1-x</sub>Ni<sub>x</sub>O<sub>3- $\delta$ </sub> redox catalysts as flexible oxygen or carbon carriers for CO<sub>2</sub> utilization and tunable production of syngas at relatively low temperatures (~700 °C), in the context of a hybrid redox process. Specifically, perovskite-structured LaFe<sub>1-x</sub>Ni<sub>x</sub>O<sub>3- $\delta$ </sub> with seven different compositions (x = 0.4 to 1) were prepared and investigated. Cyclic experiments under alternating methane and CO<sub>2</sub> flows indicated that all the samples exhibited favorable reactive performance: CH<sub>4</sub> and CO<sub>2</sub> conversions varied between 85 to 98% and 70 to 88%, respectively. While H<sub>2</sub>/CO ratio from Fe-rich redox catalysts was ~2.3:1 in the methane conversion step, Nirich catalysts produced a concentrated (~93.7 vol.%) hydrogen stream via methane cracking. The

2

flexibility of LaFe<sub>1-x</sub>Ni<sub>x</sub>O<sub>3-δ</sub> to produce syngas (or hydrogen) with tunable compositions was found

to be governed by the iron/nickel (Fe/Ni) ratio. Redox catalysts with higher Fe contents act as a

lattice oxygen carrier via chemical looping partial oxidation (CLPOx) of methane whereas those

with higher Ni contents function as a carbon carrier via chemical looping methane cracking

(CLMC) scheme. XRD analysis and temperature-programmed reactions revealed that both types

of catalysts involve the formation of La<sub>2</sub>O<sub>3</sub> and Ni<sup>0</sup>/Ni-Fe phases under the methane environment.

The ability to re-incorporate La<sub>2</sub>O<sub>3</sub> and Ni/Fe into a perovskite structure gives rise to oxygen-

carrying capacity whereas stable Ni<sup>0</sup> or Ni/Fe phases would catalyze methane cracking without

lattice oxygen exchange in the reaction cycles. Temperature programmed oxidation and Raman

spectroscopy indicated the presence of graphitic and amorphous carbon species, which were

effectively gasified by CO<sub>2</sub> to produce concentrated CO. Stability tests over LaFe<sub>0.5</sub>Ni<sub>0.5</sub>O<sub>3</sub> and

LaNiO<sub>3</sub> revealed that the redox performance was stable over a span of 50 cycles.

Keywords: CO<sub>2</sub> utilization, Syngas, Methane, Chemical Looping, Redox catalyst, Hydrogen

### 1. Introduction

Carbon dioxide (CO<sub>2</sub>) levels in the Earth's atmosphere have increased substantially due to human activities. For instance, the 2019 anthropogenic CO<sub>2</sub> emission (43 billion metric tons) has surpassed the Paris Accord's 2040 target by a factor of 2.2 Specifically, emissions from fossil fuels combustion in the industrial sector account for a quarter of the total CO<sub>2</sub> emissions in the United States in 2019.<sup>3</sup> Despite the increasing usage of renewable energy sources, fossil fuels are still expected to play a key role in fulfilling the energy requirements of our society, with a projected annualized increase of 1.4% through 2035.4 As such, the need of the hour is to develop costeffective CO<sub>2</sub> capture and utilization technologies.<sup>5,6</sup> CO<sub>2</sub> utilization offers the opportunity to produce many value-added products in chemical industries. For example, converting CO<sub>2</sub> to carbon monoxide (CO) is beneficial for a wide range of applications including the production of esters, alcohols, acids, etc. A key challenge in converting CO<sub>2</sub> to CO is breaking of the C=O bond, which is highly energy-intensive.<sup>8</sup> Photochemical and electrochemical reduction of CO<sub>2</sub> has been investigated recently but these methods still need considerable improvements to address low CO<sub>2</sub> conversion, slow electron transfer rates, and/or low photon efficiency.9 Thermochemical conversion of CO<sub>2</sub> to CO is another method in which an oxygen carrier, also known as a redox catalyst, is first thermally decomposed to release gaseous oxygen. 10-13 The (partially) reduced oxygen carrier is then exposed to CO<sub>2</sub> to produce CO by abstracting an oxygen atom from the CO<sub>2</sub> molecule while being re-oxidized. Although this approach has shown promise, the decomposition of the redox catalyst requires very high temperatures (>1100°C) and CO<sub>2</sub> conversion is low. <sup>14,15</sup> CO<sub>2</sub> can be converted to CO at relatively low temperatures (<900°C) over metal catalysts in the presence of methane, through dry reforming of methane (DRM). 16-20 The resulting product contains a mixture of hydrogen and carbon monoxide (also known as "syngas") with an H<sub>2</sub>/CO

ratio of ~1. Although DRM offers the opportunity to utilize CO<sub>2</sub>, the H<sub>2</sub>/CO ratio of the DRM syngas has limited applications. To address this limitation, we proposed an open-loop hybrid redox process (HRP) concept (Figure 1) in which a fraction of CO is essentially "extracted" from the syngas stream.<sup>21–24</sup> The key difference between DRM and HRP is that, instead of co-feeding CO<sub>2</sub> and CH<sub>4</sub>, the two gaseous reactants are exposed to an oxide based redox catalyst separately, in a two-step cyclic redox scheme (Figure 1). During the first step, CH<sub>4</sub> is partially oxidized to syngas (see R1 in Table 1) by abstracting an oxygen atom from the redox catalyst. The resulting mixture from the partial oxidation (POx) of methane has an H<sub>2</sub>/CO ratio of ~2. During the second (CO<sub>2</sub> Splitting) step, the oxygen lean redox catalyst is used to split CO<sub>2</sub> into CO, completing the redox loop. As such, syngas from the POx step can be used for the synthesis of methanol and liquid fuels.<sup>25</sup> Meanwhile, CO from the splitting step can be used separately as a feedstock for chemical production, without the need of complex syngas conditioning and separation steps.<sup>21</sup>

Redox catalyst plays a key role in the HRP process. The equilibrium conversion of  $CO_2$  splitting reaction over a redox catalyst depends on the properties of the redox material under consideration. Previous studies have shown that a low equilibrium partial pressure of oxygen ( $P_{O2}$ ) associated with a redox pair ( $MeO_x$  /  $MeO_{x-1}$ ) is favorable for high  $CO_2$  to CO conversion. Therefore, finetuning the  $P_{O2}$  value by choosing the appropriate metal oxides and varying the stoichiometric ratios is a potential way of finding a suitable candidate for effective  $CO_2$  splitting. Previous studies indicated that iron-containing redox catalysts are favorable for POx and splitting of oxidizing gases such  $CO_2$  and  $H_2O$ .  $^{16,22-24,26-28}$  For example, Bhavsar et al. investigated the redox performance and stability of nanostructured  $Fe@SiO_2$  and Fe—barium hexaaluminate (BHA) in a chemical looping dry reforming (CLDR) scheme and found that Fe—BHA showed better

stability at 800 °C, but the methane conversion was limited. <sup>16</sup> In another study, More et al. reported above 90% CH<sub>4</sub> / CO<sub>2</sub> conversions and ~95% CO selectivity at 1,000 °C via CLDR with Fe-Ni mixed oxides. <sup>29</sup> Recent experimental and density functional theory (DFT) studies have also shown

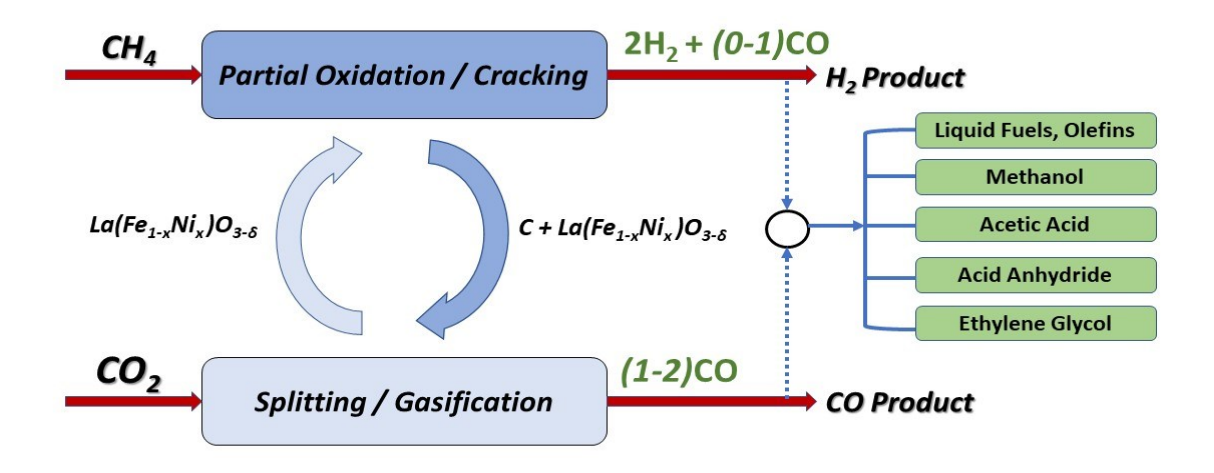


Figure 1. Simplified schematic of the hybrid redox process, with corresponding reactions shown in Table 1.

that Fe-containing perovskites, with a general formula of ABO<sub>3- $\delta$ </sub>, are suitable for CH<sub>4</sub> partial and CO<sub>2</sub> splitting. For example, Zhang et al.<sup>23</sup> reported the redox performance of nanocomposites of Sr<sub>3</sub>Fe<sub>2</sub>O<sub>7- $\delta$ </sub> and (Ca/Mn)O, which showed near 100% CO<sub>2</sub> conversion and ~96% syngas selectivity at 950 °C.

It is noted that in all the studies mentioned above, high temperatures (>800°C) were necessary to achieve high methane conversion. To enhance redox catalyst activity at low temperatures, perovskite structured LaNi<sub>0.35</sub>Fe<sub>0.65</sub>O<sub>3</sub> was mixed with rock salt structured Ce<sub>0.85</sub>Gd<sub>0.1</sub>Cu<sub>0.05</sub>O<sub>2-8</sub>. >90% conversion for both POx and CO<sub>2</sub>-splitting steps were achieved a temperature range of 700-

750 °C.<sup>22,24</sup> However, the syngas productivity per cycle (moles of synthesis gas produced per unit mass of the redox catalyst) was limited by the oxygen carrying capacity of the redox catalysts. The productivity of synthesis gas can be enhanced via a carbon carrier route. 33,34 In this aspect, methane pyrolysis (R3) is a potential approach to produce near pure hydrogen. 35-39 As indicated in R3 (Table 1), the production of hydrogen comes with the deposition of solid carbon which must be removed to regenerate the active sites of the catalyst. 40-42 To best utilize the deposited carbon in the context of HRP, CO<sub>2</sub> gasification of solid carbon to CO via a reverse-Boudouard reaction (see R4 Table 1)<sup>43</sup> is a potential way to produce highly concentrated H<sub>2</sub> and CO streams in a chemical looping methane cracking (CLMC) scheme. 33,34,44 It should be noted that, compared to an oxygen carrier, the CH<sub>4</sub> pyrolysis, and CO<sub>2</sub> gasification would require a carbon carrier. As such, the dependency on the oxygen carrying capacity is eliminated. To make R3 more efficient in terms of H<sub>2</sub> purity, a carbon carrier ideally should not have any oxygen-carrying capacity and avoid partial oxidation of CH<sub>4</sub> as well as catalyze the gasification of the solid carbon. A redox catalyst can also be designed to have both oxygen and carbon carrying functions, leading to a H<sub>2</sub>:CO ratio >2, as illustrated in Figure 1. A catalyst with both oxygen and carbon carrying capabilities can carry oxygen as indicated in R1 and R2 whereas carbon can be carried either as solid carbon (R3 and R4) or in the form of carbides. However, complete removal of carbon from carbides via CO<sub>2</sub> typically face thermodynamic and kinetic limitations.<sup>24</sup>

**Table 1:** Key reactions involved during Chemical Looping Partial Oxidation (CLPOx) and Chemical Looping Methane Cracking CLMC.

CLPOx	CLMC

$$R1: CH_4 + MeO_x \longrightarrow 2H_2 + CO + MeO_{x-1} \qquad R3: CH_4 + MeO_x \longrightarrow 2H_2 + C + MeO_x$$

$$R2: CO_2 + MeO_{x-1} \longrightarrow CO + MeO_x \qquad R4: CO_2 + C + MeO_x \longrightarrow 2CO + MeO_x$$

Recent studies have shown that Ni-based redox catalysts exhibited promising results in terms of methane decomposition. 33,34,44 More et al. 33 investigated the carbon carrying ability of Ni-doped ceria oxide (CeO<sub>2</sub>) and magnesium aluminum oxide (MgAl<sub>2</sub>O<sub>4</sub>) redox catalysts in a CLMC scheme. The results revealed that Ni-doped CeO<sub>2</sub> exhibited better performance at 900°C with both CH<sub>4</sub> and CO<sub>2</sub> conversions of ~90%. In another study, Kang et al.<sup>34</sup> used a similar approach by synthesizing Ni-dopped lanthanum oxide (La<sub>2</sub>O<sub>3</sub>) redox catalyst. In this study, CH<sub>4</sub> was introduced at 700°C while CO<sub>2</sub> at 800°C. The results of the redox experiments indicated that both CH<sub>4</sub> and CO<sub>2</sub> conversions were near 90%. Raman spectroscopy and temperature-programmed oxidation (TPO) analysis of the deposited carbon indicated the presence of graphitic carbon which was effectively gasified at 800°C. It should be noted that both More et al.<sup>33</sup> and Kang et al.<sup>34</sup> requires  $CO_2$  gasification of coke at temperatures  $\geq 800^{\circ}C$ . In addition, the carbon carriers needed to be regenerated with gaseous oxygen after several cycles due to the accumulation of graphite-like carbon. Given that amorphous carbon is more active in reacting with CO<sub>2</sub>, its preferential deposition (as opposed to graphitic carbon) may allow the CO<sub>2</sub> gasification of coke at lower temperatures (e.g. ≤ 700°C) or create a synergy between amorphous and graphitic carbon for CO<sub>2</sub> gasification. This can lead to less carbon accumulation during the long-term operations. Therefore, a carbon carrier capable of accomplishing such a function is of interest.

In this study, perovskite structured LaFe<sub>1-x</sub>Ni<sub>x</sub>O<sub>3</sub> with seven different compositions were synthesized to produce tunable syngas ratios by utilizing CO<sub>2</sub> in an open-loop hybrid redox scheme

at a relatively low temperature (700°C). Our recent studies have shown that the redox materials with a lower Ni/Fe ratio (or  $x \le 0.4$ ) exhibit favorable activity either at high temperature ( $\ge 800^{\circ}$ C) or by mixing them with other composites at low temperatures ( $\le 750^{\circ}$ C), whereas higher Ni content improves the catalyst activity at a lower temperature. In this study, the range of "x" in LaFe<sub>1-x</sub>Ni<sub>x</sub>O<sub>3</sub> was varied from 0.4 to 1. Compared to previous studies, HRP is modified by combining both CLPOx and CLMC as shown in Figure 1. The effect of the Ni/Fe ratio on product selectivity was investigated. The results of the cyclic experiments indicated that the Ni/Fe ratio in LaFe<sub>1-x</sub>Ni<sub>x</sub>O<sub>3</sub> strongly affected the balance between CLPOx and CLMC and consequently the H<sub>2</sub>/CO product compositions. Temperature-programmed reaction (TPR), X-ray diffraction (XRD), and Raman spectroscopy were conducted to investigate the underlying mechanisms involved in POx, CO<sub>2</sub> splitting, CH<sub>4</sub> decomposition, and carbon gasification assisted by LaFe<sub>1-x</sub>Ni<sub>x</sub>O<sub>3</sub>.

# 2.Experimental

# 2.1. Redox Catalyst Synthesis

LaFe<sub>1-x</sub>Ni<sub>x</sub>O<sub>3-δ</sub> perovskites with x ranging from 0.4 to 1 were synthesized via a modified Pechini method. The detailed synthesis procedure was described elsewhere.<sup>22</sup> The main synthesis steps involved the stirring of the mixture of citric acid and nitrate precursors of metals (La, Ni, and Fe) at a citric acid to the sum of the metal ions molar ratio of 2.5:1 for 30min at 40°C. The resulting cation solution was mixed with ethylene glycol by maintaining the molar ratio of ethylene glycol to citric acid at 1.5:1. The resulting mixture was then heated and stir dried at 80 °C to form a gel. This is followed by overnight heating of the gel at 120°C to form a dry solid. The dried sample was then calcined at 750 °C for six hours under an oxidizing environment. Finally, all the prepared samples were crushed and sieved to a size range of 250–450μm for redox experiments and characterizations.

## 2.2. Cyclic Tests

The redox performance of the as-prepared samples was evaluated by exposing them to five CH<sub>4</sub>/CO<sub>2</sub> redox cycles at 700°C. Approximately 0.5g of the sample was loaded inside a fixed bed (U-shaped quartz tube, 4 mm inner diameter. To keep the particles in place, the U-tube was also packed with quartz wool on both ends. The sample inside the U-tube was brought to the 700°C by placing the U-tube inside an electric furnace configured with a thermocouple to control the temperature. The inlet of the U-tube was connected to a gas delivery panel controlled by a computer for automated cyclic valve switching. The outlet of the U-tube was connected to a quadrupole mass spectrometer (Cirrus 2, MKS) to quantify the product gas compositions. The mass spec was calibrated using known concentrations of gases such as CH<sub>4</sub>, CO, CO<sub>2</sub>, H<sub>2</sub> and O<sub>2</sub>. Argon was used as an internal standard for calibration as well as calculating the amounts of product gases. Before exposing the sample to CH<sub>4</sub>/CO<sub>2</sub> redox cycles, the temperature of the electric furnace was raised to 700°C in Argon flowing at 25 mL/min (Argon flow rate was fixed during the entire redox cycle) followed by the injection of CH<sub>4</sub> at 2.8 mL/min for 2 min. After the CH<sub>4</sub> injection, the U-tube was purged with argon for 2 min before introducing CO<sub>2</sub>. During the oxidation step, CO<sub>2</sub> was injected at 1.4 mL/min for 4 min. Before the next redox cycle, the U-tube was again purged with argon for 2 min. Conversions and selectivity were calculated by using the following equations:

CH<sub>4</sub> Conversion = 100 x 
$$\frac{n_{CH_{4,in}} - n_{CH_{4,out}}}{n_{CH_{4,in}}}$$

CO<sub>2</sub> Conversion = 100 x 
$$\frac{n_{CO_{2,in}} - n_{CO_{2,out}}}{n_{CO_{2,in}}}$$

CO Selectivity (POx step) = 100 x 
$$\frac{n_{CO,out}}{n_{CO,out} + n_{CO_2,out}}$$

Isothermal redox cycles were also conducted in TGA to investigate the long-term stability and quantify the carbon deposited/gasified. ~27mg of the sample was placed inside the TGA apparatus which was heated to 700°C in Ar at 90 mL/min (Argon flow rate was fixed during the entire redox cycle). CH<sub>4</sub> and CO<sub>2</sub> were injected sequentially at 10 mL/min for 10 min. Argon was purged for 20 min between reduction and oxidation steps to remove any leftover gases. In addition, H<sub>2</sub>/CO<sub>2</sub> and H<sub>2</sub>/H<sub>2</sub>O redox cycles were also performed in the TGA to evaluate the oxygen-carrying capacity of the redox materials. The experimental conditions were the same as for CH<sub>4</sub>/CO<sub>2</sub> cycles except, 10mg of the sample was used.

## 2.2. Characterization of the Redox Catalyst

Crystalline phases present in as-prepared and spent redox catalysts were identified via X-ray diffraction (XRD). A Rigaku SmartLab X-ray diffractometer with Cu Kα radiation at 40 kV and 44 mA was used to collect the diffraction spectra. A step size of 0.05° and a residence time of 2 s at each step was used, with the 2θ angle varying from 20° to 80°. Temperature programmed reduction (TPR) experiments were conducted to examine the reduction behavior of the redox catalysts. In thermogravimetric analyzer (TGA) based TPR experiments, ~10 mg of the sample was loaded inside the TGA apparatus and exposed to a 5 vol % CH4/Ar mixture at 200ml/min with a heating rate of 10 °C/min. TPR experiments were also performed in a fixed bed (U-shaped quartz tube, 4 mm inner diameter) to observe the product gas evolutions through a mass spectrometer. ~0.2 – 0.5g of the sample was loaded inside the U-tube reactor and exposed to 20 vol % CH4/Ar mixture at 10 ml/min with a heating rate of 10°C/min. Temperature programmed oxidation (TPO) was performed in the TGA for carbon gasification. ~10mg of carbon deposited sample was loaded inside the TGA apparatus and exposed to 5 vol % CO<sub>2</sub>/Ar mixture at 200 ml/min with heating

rates ranging from 5 to 20°C/min. To further characterize the carbon species, Raman spectroscopy of the coke-deposited samples was obtained using an XploRA Plus Spectrometer with 532 nm laser. Scanning electron microscopy (SEM) was also performed using a Hitachi S3200 VPSEM with an acceleration voltage of 20 keV.

#### 3. Results and Discussion

# 3.1. Reactive Performance of the Redox Catalysts

The results from the cyclic experiments are shown in Figure 2(a). As can be seen, LaFe<sub>0.6</sub>Ni<sub>0.4</sub>O<sub>3</sub> and LaFe<sub>0.5</sub>Ni<sub>0.5</sub>O<sub>3</sub> exhibited excellent performance in terms of CH<sub>4</sub> and CO<sub>2</sub> conversions (both above 85%) with CO selectivity of  $\sim 90\%$ . The corresponding H<sub>2</sub>/CO ratios for LaFe<sub>0.6</sub>Ni<sub>0.4</sub>O<sub>3</sub> and LaFe<sub>0.5</sub>Ni<sub>0.5</sub>O<sub>3</sub> were ~2.3 as shown in Figure 2(b). This indicates little carbon formation in the methane conversion step, meaning both redox catalysts acted as an oxygen carrier under a CLPOx scheme. H<sub>2</sub>/CO ratio for LaFe<sub>0.4</sub>Ni<sub>0.6</sub>O<sub>3</sub> was also ~2.5 with CH<sub>4</sub> and CO<sub>2</sub> conversions of ~80 and 72%, respectively. Therefore, it can be inferred that the perovskite structured LaFe<sub>1-x</sub>Ni<sub>x</sub>O<sub>3</sub> with x ranging from 0.4 to 0.6 behaves primarily as an oxygen carrier. A further increase in the Ni content resulted in significantly higher H<sub>2</sub>/CO ratios of ~6, 7, and 9 for LaFe<sub>0.3</sub>Ni<sub>0.7</sub>O<sub>3</sub>, LaFe<sub>0.2</sub>Ni<sub>0.8</sub>O<sub>3</sub>, and LaFe<sub>0.1</sub>Ni<sub>0.9</sub>O<sub>3</sub>. The corresponding CH<sub>4</sub> and CO<sub>2</sub> conversions varied between 82 -95% and 70-78%, respectively Complete elimination of Fe resulted in an H<sub>2</sub>/CO ratio of 16 with 90% CH<sub>4</sub> conversion and 85% CO<sub>2</sub> conversion. This indicates that LaNiO<sub>3</sub> has a negligible oxygen-carrying capacity as most of the methane was cracked, producing a highly concentrated H<sub>2</sub>. It should be noted from Figure 2(a) that CO concentration during the CO<sub>2</sub> step varied between 75 to 90% for all the LaFe<sub>1-x</sub>Ni<sub>x</sub>O<sub>3</sub> samples tested, confirming the ability to produce a concentrated CO stream and a separate hydrogen or syngas stream with varying compositions. Although the CO rich product has a small fraction of CO<sub>2</sub>, it can be purified with standard technologies such as acid gas

removal<sup>49,50</sup> and pressure swing adsorption.<sup>51</sup> In addition, the presence of small amount of CO<sub>2</sub> in CO can be beneficial for some specific industrial applications such as methanol synthesis.<sup>52</sup>

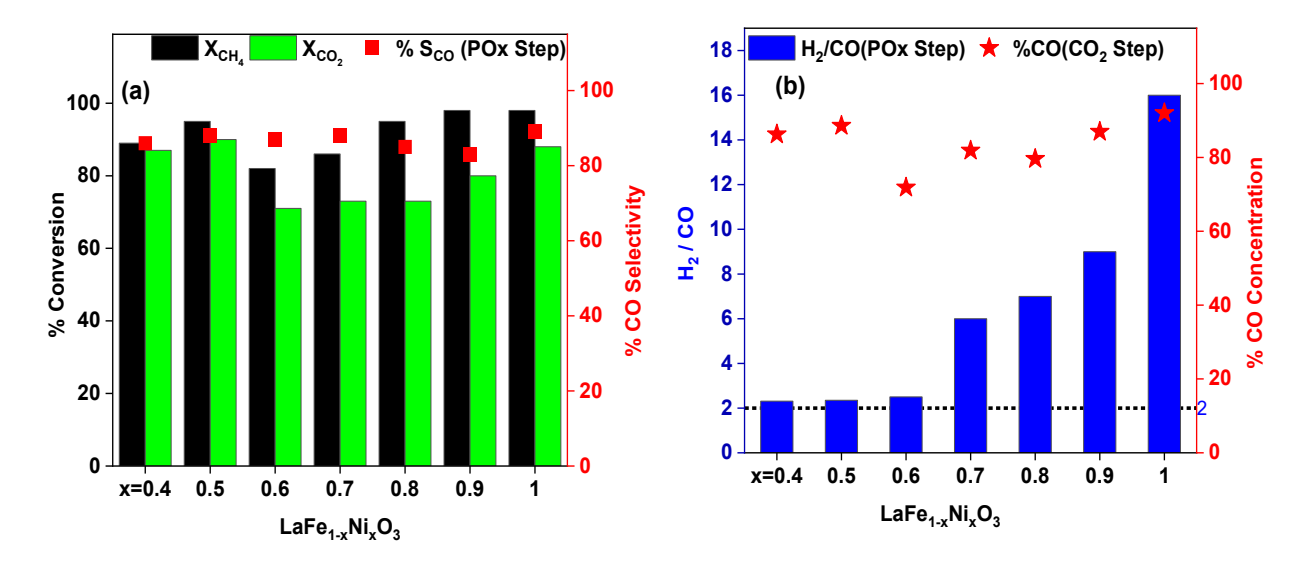


**Figure 2.** Redox performance of LaFe<sub>1-x</sub>Ni<sub>x</sub>O<sub>3</sub> (x = 0.4-1) at 700 °C: (a) CH<sub>4</sub> conversion and CO selectivity in the methane step and CO<sub>2</sub> conversion in the regeneration step; and (b) H<sub>2</sub>/CO ratio in the methane step and CO concentration in the CO<sub>2</sub> regeneration step. (Note: The uncertainty in the carbon and oxygen balances were less than 5%)

Carbon and oxygen balances indicated that the materials with higher Fe content such as LaFe<sub>0.6</sub>Ni<sub>0.4</sub>O<sub>3</sub> and LaFe<sub>0.5</sub>Ni<sub>0.5</sub>O<sub>3</sub> mainly partially oxidized CH<sub>4</sub> while the conversion of CO<sub>2</sub> to CO was dominant by lattice oxygen replenishment. On the other hand, materials with lower Fe contents such as LaFe<sub>0.1</sub>Ni<sub>0.9</sub>O<sub>3</sub> and LaNiO<sub>3</sub> favored catalytic decomposition of CH<sub>4</sub> by depositing carbon on the redox catalyst while the conversion of CO<sub>2</sub> to CO was dominant by the gasification of the deposited carbon. Therefore, it can be inferred that the flexibility of LaFe<sub>1-x</sub>Ni<sub>x</sub>O<sub>3-\delta</sub> to produce a tunable syngas ratio is governed by the amount of oxygen/carbon circulating between CH<sub>4</sub> and CO<sub>2</sub> steps which seems to be controlled by the Fe/Ni ratio. The next section further

characterizes the perovskite structured LaFe<sub>1-x</sub>Ni<sub>x</sub>O<sub>3- $\delta$ </sub> redox catalysts in terms of their reduction/oxidation behaviors and phase transformation during the reduction and oxidation steps.

# 3.2. Sample characterizations

To better understand the flexible nature of LaFe<sub>1-x</sub>Ni<sub>x</sub>O<sub>3-δ</sub>, we selected LaFe<sub>0.5</sub>Ni<sub>0.5</sub>O<sub>3</sub> (LNF) and LaNiO<sub>3</sub> (LN) to study the reduction and oxidation behaviors and quantify the oxygen-carrying capacity. The reduction behaviors of LNF and LN are presented in the Figure 3 where Figure 3(a) represents the H<sub>2</sub>-TPR profiles and Figure 3(b) and Figure 3(c) represent the cumulative lattice oxygen release and carbon deposited (calculated from gas evolutions during CH<sub>4</sub>-TPR in packed bed, see Figure S1), respectively. Based on H<sub>2</sub>/CH<sub>4</sub>-TPR results, the reduction behavior of both LNF and LN can be divided into two zones: Zone-1 (200-450 $^{\circ}$ C) and Zone-2 (450 – 800 $^{\circ}$ C). As can been seen from Figure 3(b) and Figure 3(c), there were negligible amounts of oxygen release and carbon deposited in Zone-1 during CH<sub>4</sub>-TPR of both LNF and LN. However, two low temperature peaks can be observed during H<sub>2</sub>-TPR for both LNF and LN. This can be attributed to the difficulty in CH<sub>4</sub> activation at low temperatures. The first low temperature peak in Zone-1 during H<sub>2</sub>-TPR at around 250°C and 320°C for LNF and LN respectively can be assigned to the removal of chemisorbed oxygen in the vacancies of the perovskite structure.<sup>53</sup> Second reduction peak (~362°C) in Zone-1 for LN during H<sub>2</sub>-TPR can be assigned to the transformation of LaNiO<sub>3</sub> into La<sub>4</sub>Ni<sub>3</sub>O<sub>10</sub> according to the following reaction:

$$4LaNiO_3 + 2H_2 \rightarrow La_4Ni_3O_{10} + Ni^o + 2H_2O$$

Whereas the second reduction peak during H<sub>2</sub>-TPR for LNF (~393°C) is broader, likely due to the complexity resulting from a co-presence of Ni and Fe.<sup>54</sup> In Zone-2, two reduction peaks were

observed for LN which can be assigned to the further transformation of La<sub>4</sub>Ni<sub>3</sub>O<sub>10</sub> into La<sub>2</sub>NiO<sub>4</sub> and La<sub>2</sub>O<sub>3</sub> respectively, as shown in the following reactions.

$$\begin{split} La_4Ni_3O_{10} + 3H_2 &\to La_2NiO_4 + 2Ni^o + La_2O_3 + 3H_2O \\ La_2NiO_4 + 3H_2 &\to 2La_2O_3 + 3Ni^o + 3H_2O \end{split}$$

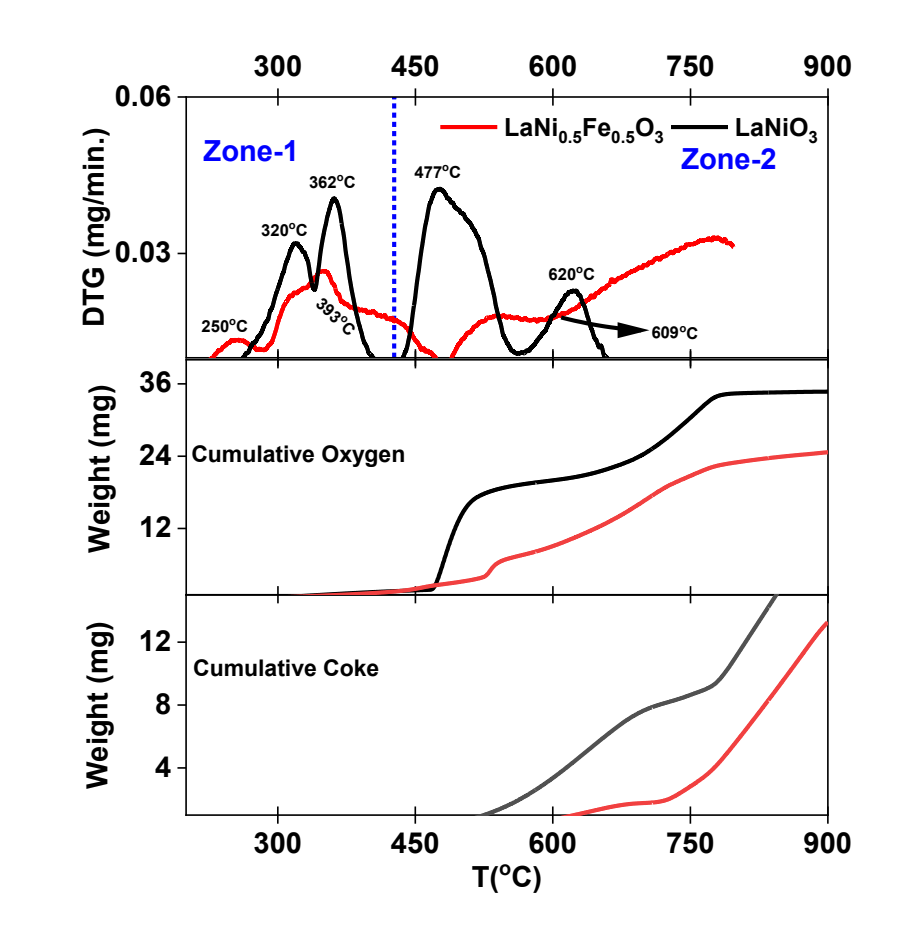


Figure 3. (a) Derivative weigh change (DTG) during  $H_2$  TPR of LaNiO<sub>3</sub> and LaFe<sub>0.5</sub>Ni<sub>0.5</sub>O<sub>3</sub> in TGA; (b) cumulative oxygen release and (c) cumulative coke deposited during  $CH_4$ -TPR in a packed bed.

It is clear form Figure 3(b) and Figure 3(c) that during these two transformation stages in Zone-2, oxygen was released first (at 477 and 620°C) followed by the deposition of coke which is largely due the presence of metallic Ni. Batiot et al.<sup>53</sup> have also confirmed the existence of La<sub>4</sub>Ni<sub>3</sub>O<sub>10</sub> and La<sub>2</sub>NiO<sub>4</sub> phases along with Ni° with the help of in-situ XRD conducted under reducing

environment. The third reduction peak for LNF during H<sub>2</sub>-TPR was shifted to a higher temperature (compared to 477°C peak of LN) which is broader and centered at 609°C due to the incorporation of Fe. This indicates that the partial incorporation of Fe tends not to favor the complete reduction of Ni and Fe, compared to the formation of Ni<sup>o</sup> and La<sub>2</sub>O<sub>3</sub> in LaNiO<sub>3</sub>. However, a small fraction of the Fe can nevertheless gets reduced to form a Ni-Fe alloy. <sup>22,24,55</sup> It is also worth noting that in Zone-2, LNF continue to release its active lattice oxygen, which is suitable for methane POx as evident from the H<sub>2</sub> / CO ratio (~2.3) of the product gas (Figure S1) with minimal coke formation at <750°C when compared to LN. Although as-prepared LN can be reduced, it cannot be reoxidized by CO<sub>2</sub> as confirmed by isothermal H<sub>2</sub>/CO<sub>2</sub> and H<sub>2</sub>/H<sub>2</sub>O cycles shown in Figure S2. *In*situ XRD (Figure S3) as well as isothermal H<sub>2</sub>/CO<sub>2</sub> cycles (Figure S2) also indicate that LN can absorb a small amount of the CO<sub>2</sub> onto La<sub>2</sub>O<sub>3</sub> in the form lanthanum oxycarbonate (La<sub>2</sub>O<sub>2</sub>CO<sub>3</sub>).<sup>56</sup> In comparison, LNF exhibits an isothermal oxygen storage capacity of 1.7 wt.%. These results indicate that, at the proposed operating temperature window of 650 - 750°C, LN would function as a carbon carrier whereas LNF would primarily function as an oxygen carrier. This is consistent with the cyclic testing results shown in Figure 2. We also note that the TPR was conducted with as-prepared, fully oxidized samples. Under the working conditions, CO<sub>2</sub>-reoxidation cannot reoxidize the redox catalysts to their full extent, particularly for samples with high Ni loadings.

Figure 4 summarizes the XRD spectra of the as-prepared and cycled LNF samples. For all the as-prepared LaFe<sub>1-x</sub>Ni<sub>x</sub>O<sub>3- $\delta$ </sub> samples, an orthorhombic perovskite phase was detected with negligible impurities. XRD patterns of cycled LaNi<sub>1-x</sub>Fe<sub>x</sub>O<sub>3</sub> samples at various Ni loadings are shown in Figure 4(b). It can be observed from Figure 4(b) that, upon reduction, LaNiO<sub>3</sub> was reduced to Ni and La<sub>2</sub>O<sub>3</sub> phase and CO<sub>2</sub> regeneration cannot restore the original perovskite structure. In

comparison, for LNF samples with relatively larger Fe loadings ( $x\le0.7$ ), the perovskite phase was still present after the reaction, along with bimetallic Ni/Fe phases and La<sub>2</sub>O<sub>3</sub> phase.

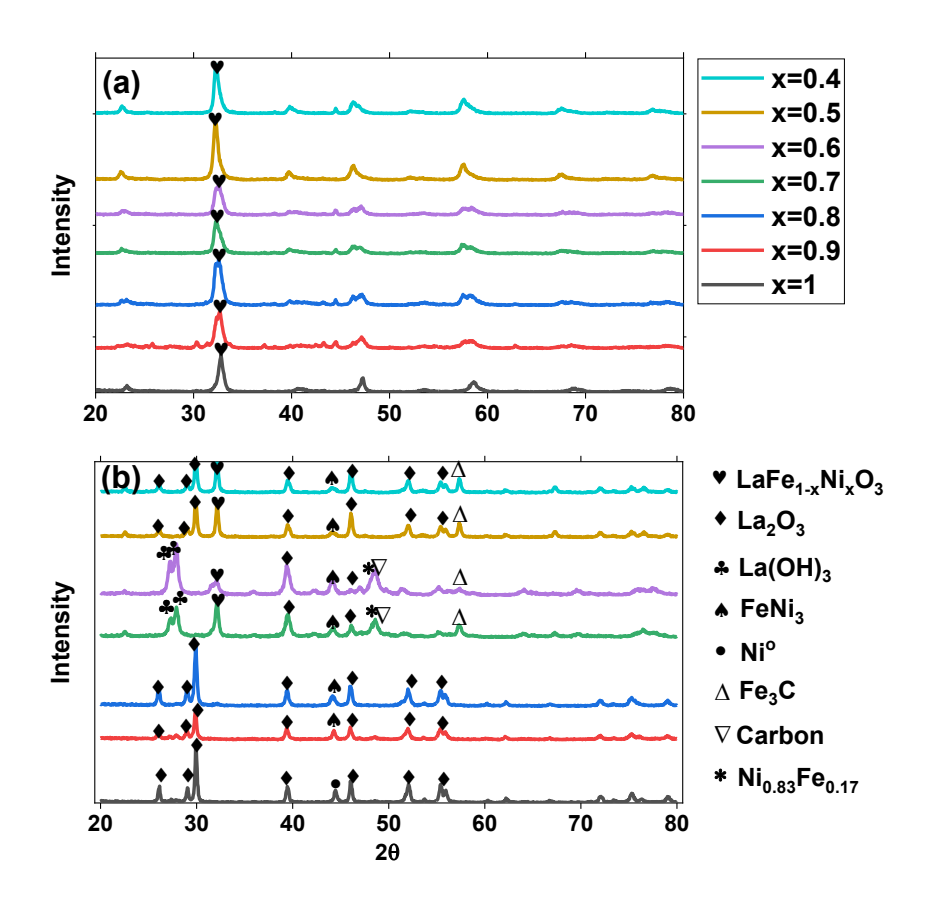


**Figure 4.** XRD patterns of (a) as-synthesized and (b) cycled  $LaFe_{1-x}Ni_xO_3$  ending after the  $CO_2$  step.

To further determine the reactive behavior of LNF and LN samples under cyclic methane and CO<sub>2</sub> environments, the XRD spectra of LaFe<sub>0.5</sub>Ni<sub>0.5</sub>O<sub>3</sub> and LaNiO<sub>3</sub> samples ending in the CH<sub>4</sub> and CO<sub>2</sub> steps are shown in the Figure 5(a & b). Under the working state, LaNiO<sub>3</sub> was decomposed to Ni<sup>o</sup> and La<sub>2</sub>O<sub>3</sub> phases with average crystallite sizes of ~51 and 40nm, respectively. They remained unchanged during the CH<sub>4</sub> and CO<sub>2</sub> steps, indicating that Ni<sup>o</sup> remained in its metallic state and consistent with the lack of oxygen carrying capacity. The presence of La(OH)<sub>3</sub> was resulted from exposure to the moisture in the environment, as confirmed by in-situ XRD (Figure S3). The

presence of graphitic carbon in the post methane LN sample confirms coke formation in the methane step. In comparison, LNF showed a predominant perovskite phase after CO<sub>2</sub>-regeneration with a small amount of La<sub>2</sub>O<sub>3</sub> and metallic Ni/Fe phases. Upon methane reduction, the intensity of the peaks associated with the perovskite phase decreased whereas La<sub>2</sub>O<sub>3</sub> and Ni/Fe phases became more prominent. A slight peak shift can be observed for the perovskite phase, most probably due to the change in B-site cation compositions resulted from Ni/Fe segregation and reincorporation into the perovskite structure. These phase compositions indicate that LaFe<sub>1-x</sub>Ni<sub>x</sub>O<sub>3-δ</sub> donates its lattice oxygen primarily by partially decomposing into La<sub>2</sub>O<sub>3</sub> and bimetallic Ni/Fe phases. The removed lattice oxygen is then replenished back via the CO<sub>2</sub> splitting step where La<sub>2</sub>O<sub>3</sub> and Ni-Fe are partially merged back. This behavior is consistent with the findings in recent studies.<sup>22,55</sup>

Figure 4(b) also indicated iron carbide (Fe<sub>3</sub>C) formation. However, it had minimal effect on the long-term performance of the redox catalyst, as will be discussed in the Section 3.3. Our previous study also indicated that the iron carbide phase can be periodically removed by air re-oxidation.<sup>24</sup> Furthermore, materials with Fe mole fraction on the B-site ranging from 0.6 to 0.7 were decomposed into additional phases such as Ni<sub>0.83</sub>Fe<sub>0.17</sub>, as shown the Figure 4(b). The existence of these additional phases affected both CH<sub>4</sub> and CO<sub>2</sub> conversions as can be seen from the Figure 2(a). The re-formation of the perovskite structured LaFe<sub>1-x</sub>Ni<sub>x</sub>O<sub>3-\delta</sub> is more likely for the redox material with higher Fe loading, this corresponds to higher oxygen-carrying capacity and lower carbon carrying capacity. Redox catalysts with higher Ni-loading (x=0.8 to 1), on the other hand, cannot be effectively re-oxidized by CO<sub>2</sub> to restore the perovskite phase. As such, they primarily act as carbon carriers and produces concentrated H<sub>2</sub> in the methane step. Considering the above

discussion, we can infer that the reaction mechanisms for both CLPOx and CLMC involve the formation of La<sub>2</sub>O<sub>3</sub> and Ni<sup>o</sup> /Ni-Fe phases. The ability to re-incorporate La<sub>2</sub>O<sub>3</sub> and Ni/Fe into a perovskite structure gives rise to oxygen carrying capacity whereas stable Ni<sup>o</sup> or Ni/Fe phases would catalyze methane cracking without lattice oxygen exchange in the reaction cycles. The balance between CLPOx and CLMC is tuned by controlling the Ni-Fe ratio that ultimately allows the tunable syngas production.

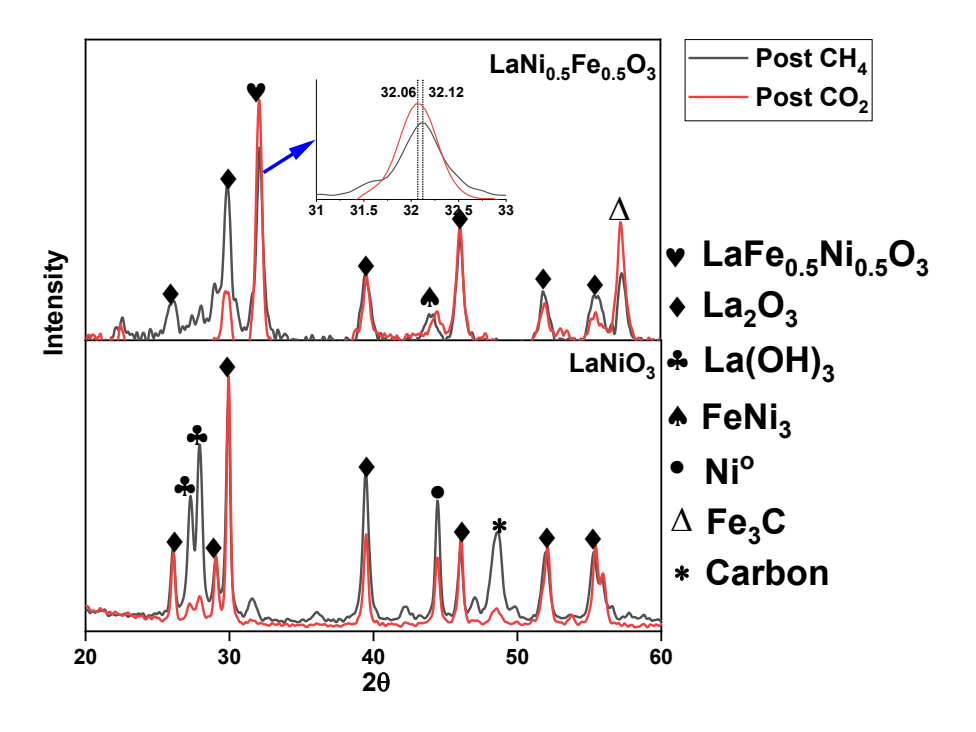
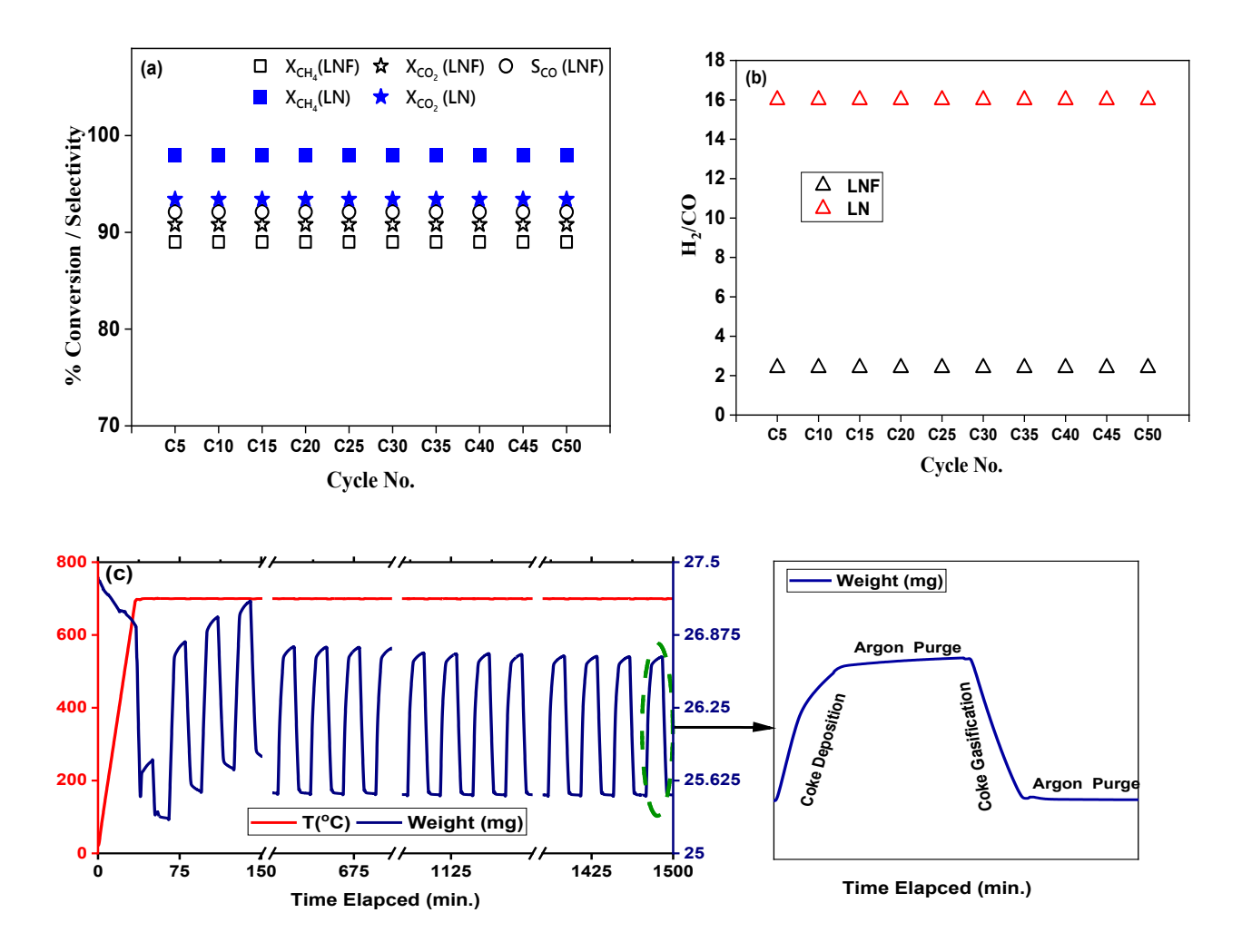


Figure 5. XRD patterns of post CH<sub>4</sub> and post-CO<sub>2</sub> after 50 reaction cycles: (a) LaFe<sub>0.5</sub>Ni<sub>0.5</sub>O<sub>3</sub> and (b) LaNiO<sub>3</sub>

### 3.3. Long term stability tests

Long-term stability tests were conducted by exposing LaFe<sub>0.5</sub>Ni<sub>0.5</sub>O<sub>3</sub> and LaNiO<sub>3</sub> to 50 redox cycles in a packed bed reactor. The results are presented in the Figure 6. As can be seen, the redox performance of both LaFe<sub>0.5</sub>Ni<sub>0.5</sub>O<sub>3</sub> and LaNiO<sub>3</sub> were stable throughout the 50 cycles. The stability can also be confirmed by XRD patterns of the cycled samples (Figure 5). A very small amount of iron carbide (Fe<sub>3</sub>C) can be observed from the XRD patterns. The quantitative analysis suggested

that carbon accumulation in the form of Fe<sub>3</sub>C is less than 0.05 wt.%, which had a minimal effect on the overall performance. To quantify the carbon carrying capacity, 50 isothermal CH<sub>4</sub>/CO<sub>2</sub> cycles were conducted over LaNiO<sub>3</sub> in TGA. The results are shown in the Figure 6(c). As can be seen, after the first three cycles, a steady state performance was achieved, as evident from the amount of carbon deposited (~1.2mg) being equal to the amount of carbon removed each cycle. A weight gain/loss of 1.2 mg corresponds to ~ 4.5 wt.% equivalent oxygen capacity, much higher than the oxygen capacity of typical redox catalysts for CO<sub>2</sub>-splitting and methane conversion. 30,57,58 Coke built up during the long-term operation has the tendency of blocking the active sites which may increase pressure in the fixed bed. Such pressure built up can be avoided my limiting the CH<sub>4</sub> injection and gasifying coke on regular intervals. The cyclic nature of HRP allows the cyclic coke removal. It can be seen from Figure 6 that both CH<sub>4</sub> and CO<sub>2</sub> conversions were stable throughout the 50 cycles, indicating that the net coke deposition was not causing any performance issues. A small amount of coke accumulated at the end can nevertheless be removed via air treatment. In the current study, we focused on a fixed bed configuration. However, this can also be realized in fluidized beds.<sup>59,60</sup> To circumvent the defluidization in the fluidized bed reactors, controlling the sintering temperature and optimizing the particle size to avoid agglomeration are important.<sup>59</sup>



**Figure 6.** Long-term redox performance of LaFe<sub>0.5</sub>Ni<sub>0.5</sub>O<sub>3</sub> and LaNiO<sub>3</sub> in packed bed (a) CH<sub>4</sub> and CO<sub>2</sub> conversions and CO selectivity and (b)  $H_2$ /CO ratios; (c) Carbon deposition/gasification cycles over LaNiO<sub>3</sub> in TGA.

# 3.4. Characterization of the carbon species

Given the attractive performance of LN as a carbon carrier, the nature and reactivity of the solid carbon deposited were examined with the aid of temperature-programmed oxidation (TPO) and Raman spectroscopy. Two pre-reduced LN samples ending in CH<sub>4</sub> and CO<sub>2</sub> steps were prepared. The carbon deposited samples (Post-CH<sub>4</sub>) was exposed to CO<sub>2</sub> at various ramping rates in TGA. The results of the TPO experiments (Figure 7(a)) indicated the presence of three peaks. The low-temperature peak (546°C) corresponds to amorphous carbon ( $C_{\alpha}$ ), which can be gasified by CO<sub>2</sub>

relatively easily whereas the high-temperature peak at around 720°C corresponds to the less active graphitic carbon ( $C_{\beta}$ ).  $^{61,62}$  The results of the cyclic tests (Figure 2) indicated that both  $C_{\alpha}$  and  $C_{\beta}$  were effectively converted under the reaction conditions, showing 85% CO<sub>2</sub> conversion at 700 °C. It may also be noted from the TPO results that LN ending in the CO<sub>2</sub> step does not show any peak below 720°C. This confirms that most of the deposited carbon was removed by the CO<sub>2</sub> step. A minor peak at around 770°C can be observed, which is likely to be due to a small amount of highly stable carbon species that cannot be effectively removed by CO<sub>2</sub> under 700 °C isothermal operations. Activation energies for the CO<sub>2</sub> gasification of  $C_{\alpha}$  and  $C_{\beta}$  were calculated using the Kissinger method:

$$ln(\gamma T_o^{-2}) = -E_a(RT_o)^{-1} + ln(AR E_a^{-1})$$

Where  $\gamma$ ,  $T_p$ , A, R and  $E_a$  represents the heating rate (°C/min), peak temperature (K), preexponential factor, general gas constant(J/mol.K), and the activation energy (kJ/mol), respectively. Various heating rates and peak temperatures from the Figure 7(a) were fitted to determine the activation energies for the  $CO_2$  gasification of  $C_\alpha$  and  $C_\beta$  (see Figure S3 in the supplemental file). The activation energies calculated are 53 and 83 kJ/mol for  $C_\alpha$  and  $C_\beta$  respectively, further confirming that  $C_\alpha$  is more reactive with  $CO_2$ .

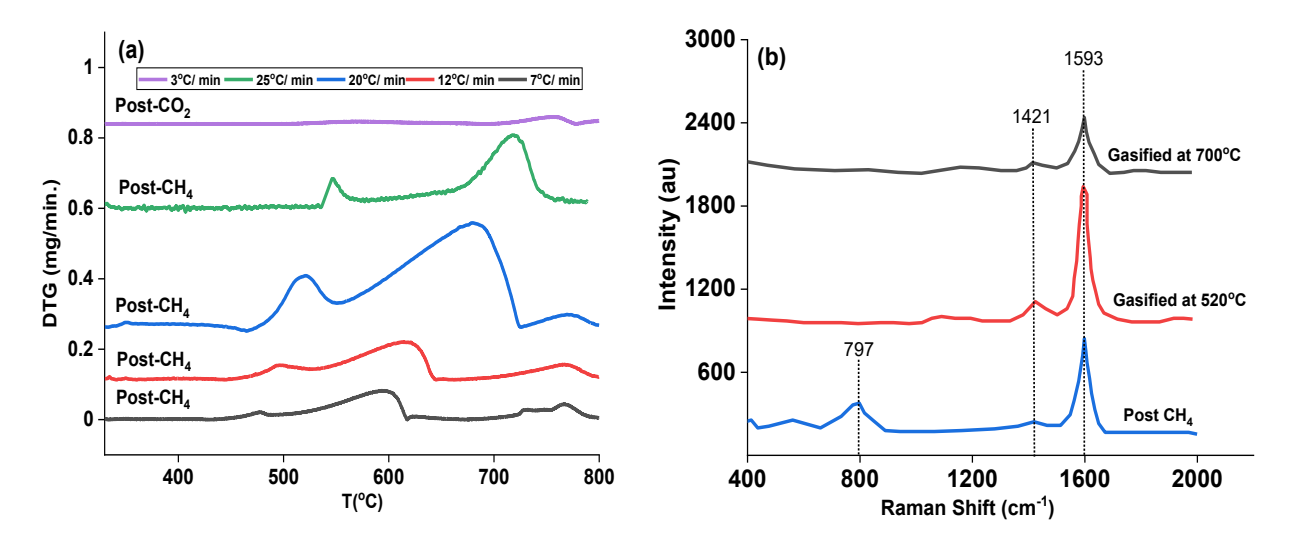


Figure 7. (a) Weight loss peaks of the during CO<sub>2</sub> -TPO, (b) Raman spectra of coke depleted and CO<sub>2</sub>-Gasified samples.

Raman spectroscopy was used to confirm the nature of all types of carbons. Based on the TPO results, three samples S1 (Post-CH<sub>4</sub>), S2 (CO<sub>2</sub> gasification of S1 at 520°C), and S3 (CO<sub>2</sub> gasification of S1 at 700°C) were prepared. As seen in Figure 7(b), three major peaks appeared at 797, 1421, and 1593cm<sup>-1</sup> respectively for the three samples (S1, S2, and S3). The peak at around 797cm<sup>-1</sup> most likely corresponds to the amorphous carbon<sup>63</sup> (C<sub> $\alpha$ </sub>), which disappeared for S2 indicating the selective oxidation of C<sub> $\alpha$ </sub> at relatively low temperatures. The peak at 1593 cm<sup>-1</sup> corresponds to the G-band of graphite whereas the peak at 1421cm<sup>-1</sup> (shifted by ~51cm<sup>-1</sup> compared to a typical D-band at 1370cm<sup>-1</sup> due to UV excitation<sup>64</sup>) belongs to the defects in the graphite structure (D-band).<sup>65</sup> The intensities of both D and G bands decreased for S3 compared to S2, indicating that most of the carbon was gasified at 700°C. The presence of both bands for S3 also indicates that there is still some leftover, stable carbon species. This corresponds well with the TPO data of the post-CO<sub>2</sub> sample in Figure 7a, which showed a peak at 770°C. It is also worth noting that the synergy between C<sub> $\alpha$ </sub> and C<sub> $\beta$ </sub> leads to better overall CO<sub>2</sub> conversion, and further optimization of the deposited carbon species can lead to improved CLMC performance.

# Conclusion

The present study reports LaFe<sub>1-x</sub>Ni<sub>x</sub>O<sub>3- $\delta$ </sub> redox catalysts (0.4  $\leq$  x  $\leq$  1) as flexible oxygen or carbon carriers for CO<sub>2</sub> utilization and tunable production of syngas at relatively low temperatures (~700°C) in the context of a hybrid redox process. Among them, redox catalysts with higher Fe contents exhibited promising results in terms of their oxygen carrying capability for chemical looping partial oxidation (CLPOx) of methane. In comparison, redox catalysts with higher Ni contents primarily function as carbon carriers for chemical looping methane cracking (CLMC). XRD and TPR characterizations revealed that both CLPOx and CLMC involve the formation of La<sub>2</sub>O<sub>3</sub> and Ni<sup>0</sup>/Ni-Fe phases. The ability to re-incorporate La<sub>2</sub>O<sub>3</sub> and Ni/Fe into a perovskite structure gives rise to oxygen carrying capacity whereas stable Ni<sup>0</sup> or Ni/Fe phases would catalyze methane cracking with negligible lattice oxygen exchange in the reaction cycles. The balance between CLPOx and CLMC can be tuned by controlling the Ni-Fe ratio that ultimately allows tunable syngas production. Temperature programed oxidation and Raman spectroscopy of the carbon carrier (LaNiO<sub>3-δ</sub>) indicated the presence of graphitic and amorphous carbon, which can be effectively gasified by CO<sub>2</sub> to produce a concentrated carbon monoxide stream. Stability tests over LaFe<sub>0.5</sub>Ni<sub>0.5</sub>O<sub>3</sub> and LaNiO<sub>3</sub> revealed that the redox performance was stable over span of 50 cycles.

# Acknowledgement

This work was supported by the U.S. Department of Energy (Award DE-FE0031703), the National Science Foundation (CBET- 1923468), and the North Carolina State University Kenan Institute for Engineering, Technology and Science. The authors acknowledge the use of the Analytical Instrumentation Facility (AIF) at North Carolina State University, which is supported by the State of North Carolina and the National Science Foundation. The Raman study was conducted as part of a user project at the Center for Nanophase Materials Sciences (CNMS), which is a US Department of Energy, Office of Science User Facility at Oak Ridge National Laboratory.

### References

- (1) Intergovernmental Panel on Climate Change (IPCC). Carbon Dioxide Capture and Storage; Metz, B., Davidson, O., de Coninck, H., Loos, M., Meyer, L., Eds.; Cambridge University Press: Cambridge, U.K., 2005; pp 431.
- (2) Newell, R. G.; Raimi, D.; Aldana, G. Global Energy Outlook 2019: The Next Generation of Energy; Resources for the Future (RFF): Washington, D.C., July 2019; Report 19-06, <a href="https://media.rff.org/documents/GEO\_Report\_8-22-19.pdf">https://media.rff.org/documents/GEO\_Report\_8-22-19.pdf</a> (accessed on 06/04/2021).
- (3) United States Environmental Protection Agency (U.S. EPA).Inventory of U.S. Greenhouse Gas Emissions and Sinks; U.S. EPA: Washington, D.C., 2021; <a href="https://www.epa.gov/ghgemissions/inventory-us-greenhouse-gas-emissions-and-sinks">https://www.epa.gov/ghgemissions/inventory-us-greenhouse-gas-emissions-and-sinks</a> (accessed on 06/ 04/2021).
- (4) Birol, F. World Energy Outlook 2012; International Energy Agency (IEA): Paris, France, 2012; <a href="https://www.iea.org/reports/world-energy-outlook-2012">https://www.iea.org/reports/world-energy-outlook-2012</a> (accessed on 06/04/2021).
- (5) Ho, H.-J.; Iizuka, A.; Shibata, E. Carbon Capture and Utilization Technology without Carbon Dioxide Purification and Pressurization: A Review on Its Necessity and Available Technologies. *Ind. Eng. Chem. Res.* **2019**, *58* (21), 8941–8954. https://doi.org/10.1021/acs.iecr.9b01213.
- (6) Mukherjee, A.; Okolie, J. A.; Abdelrasoul, A.; Niu, C.; Dalai, A. K. Review of Post-Combustion Carbon Dioxide Capture Technologies Using Activated Carbon. *Journal of Environmental Sciences* **2019**, *83*, 46–63. https://doi.org/10.1016/j.jes.2019.03.014.

- (7) Du, C.; Lu, P.; Tsubaki, N. Efficient and New Production Methods of Chemicals and Liquid Fuels by Carbon Monoxide Hydrogenation. *ACS Omega* **2020**, *5* (1), 49–56. https://doi.org/10.1021/acsomega.9b03577.
- (8) Mesters, C. A Selection of Recent Advances in C1 Chemistry. *Annu. Rev. Chem. Biomol. Eng.* **2016**, 7 (1), 223–238. https://doi.org/10.1146/annurev-chembioeng-080615-034616.
- (9) Peter, S. C. Reduction of CO <sub>2</sub> to Chemicals and Fuels: A Solution to Global Warming and Energy Crisis. *ACS Energy Lett.* **2018**, *3* (7), 1557–1561. https://doi.org/10.1021/acsenergylett.8b00878.
- (10) Muhich, C.; Steinfeld, A. Principles of Doping Ceria for the Solar Thermochemical Redox Splitting of H<sub>2</sub> O and CO<sub>2</sub>. *J. Mater. Chem. A* **2017**, *5* (30), 15578–15590. https://doi.org/10.1039/C7TA04000H.
- (11) Carrillo, A. J.; Bork, A. H.; Moser, T.; Sediva, E.; Hood, Z. D.; Rupp, J. L. M. Modifying La <sub>0.6</sub> Sr <sub>0.4</sub> MnO <sub>3</sub> Perovskites with Cr Incorporation for Fast Isothermal CO <sub>2</sub> -Splitting Kinetics in Solar-Driven Thermochemical Cycles. *Adv. Energy Mater.* **2019**, *9* (28), 1803886. https://doi.org/10.1002/aenm.201803886.
- (12) Furler, P.; Scheffe, J.; Marxer, D.; Gorbar, M.; Bonk, A.; Vogt, U.; Steinfeld, A. Thermochemical CO<sub>2</sub> Splitting *via* Redox Cycling of Ceria Reticulated Foam Structures with Dual-Scale Porosities. *Phys. Chem. Chem. Phys.* **2014**, *16* (22), 10503–10511. https://doi.org/10.1039/C4CP01172D.
- (13) Arifin, D.; Aston, V. J.; Liang, X.; McDaniel, A. H.; Weimer, A. W. CoFe2O4 on a Porous Al2O3 Nanostructure for Solar Thermochemical CO2 Splitting. *Energy Environ. Sci.* **2012**, *5* (11), 9438. https://doi.org/10.1039/c2ee22090c.
- (14) Chueh, W. C.; Falter, C.; Abbott, M.; Scipio, D.; Furler, P.; Haile, S. M.; Steinfeld, A. High-Flux Solar-Driven Thermochemical Dissociation of CO2 and H2O Using Nonstoichiometric Ceria. *Science* **2010**, *330* (6012), 1797–1801. https://doi.org/10.1126/science.1197834.
- (15) Al-Shankiti, I.; Ehrhart, B. D.; Weimer, A. W. Isothermal Redox for H 2 O and CO 2 Splitting A Review and Perspective. *Solar Energy* **2017**, *156*, 21–29. https://doi.org/10.1016/j.solener.2017.05.028.
- (16) Bhavsar, S.; Najera, M.; Veser, G. Chemical Looping Dry Reforming as Novel, Intensified Process for CO2 Activation. *Chem. Eng. Technol.* **2012**, *35* (7), 1281–1290. https://doi.org/10.1002/ceat.201100649.
- (17) Araiza, D. G.; Arcos, D. G.; Gómez-Cortés, A.; Díaz, G. Dry Reforming of Methane over Pt-Ni/CeO2 Catalysts: Effect of the Metal Composition on the Stability. *Catalysis Today* **2021**, *360*, 46–54. https://doi.org/10.1016/j.cattod.2019.06.018.

- (18) Kang, D.; Lim, H. S.; Lee, J. W. Mesoporous Fe <sub>2</sub> O <sub>3</sub> –CeO <sub>2</sub> –Al <sub>2</sub> O <sub>3</sub> Oxygen Carrier for Chemical Looping Dry Reforming with Subsequent Water Splitting. *Ind. Eng. Chem. Res.* **2020**, *59* (36), 15912–15920. https://doi.org/10.1021/acs.iecr.0c03197.
- (19) Hosseini, D.; Abdala, P. M.; Donat, F.; Kim, S. M.; Müller, C. R. Bifunctional Core-Shell Architecture Allows Stable H2 Production Utilizing CH4 and CO2 in a Catalytic Chemical Looping Process. *Applied Catalysis B: Environmental* **2019**, *258*, 117946. https://doi.org/10.1016/j.apcatb.2019.117946.
- (20) Bhattar, S.; Abedin, Md. A.; Kanitkar, S.; Spivey, J. J. A Review on Dry Reforming of Methane over Perovskite Derived Catalysts. *Catalysis Today* **2021**, *365*, 2–23. https://doi.org/10.1016/j.cattod.2020.10.041.
- (21) Haribal, V. P.; Wang, X.; Dudek, R.; Paulus, C.; Turk, B.; Gupta, R.; Li, F. Modified Ceria for "Low-Temperature" CO <sub>2</sub> Utilization: A Chemical Looping Route to Exploit Industrial Waste Heat. *Adv. Energy Mater.* **2019**, *9* (41), 1901963. https://doi.org/10.1002/aenm.201901963.
- (22) Jiang, Q.; Gao, Y.; Haribal, V. P.; Qi, H.; Liu, X.; Hong, H.; Jin, H.; Li, F. Mixed Conductive Composites for 'Low-Temperature' Thermo-Chemical CO2 Splitting and Syngas Generation. *J. Mater. Chem. A* **2020**, *8* (26), 13173–13182. https://doi.org/10.1039/D0TA03232H.
- (23) Zhang, J.; Haribal, V.; Li, F. Perovskite Nanocomposites as Effective CO <sub>2</sub> -Splitting Agents in a Cyclic Redox Scheme. *Sci. Adv.* **2017**, *3* (8), e1701184. https://doi.org/10.1126/sciadv.1701184.
- (24) Iftikhar, S.; Jiang, Q.; Gao, Y.; Liu, J.; Gu, H.; Neal, L.; Li, F. LaNi  $_x$  Fe  $_{1-x}$  O  $_{3-\delta}$  as a Robust Redox Catalyst for CO  $_2$  Splitting and Methane Partial Oxidation. *Energy Fuels* **2021**, *35* (17), 13921–13929. https://doi.org/10.1021/acs.energyfuels.1c02258.
- (25) Teimouri, Z.; Abatzoglou, N.; Dalai, A. K. Kinetics and Selectivity Study of Fischer—Tropsch Synthesis to C5+ Hydrocarbons: A Review. *Catalysts* **2021**, *11* (3), 330. https://doi.org/10.3390/catal11030330.
- (26) Michalsky, R.; Neuhaus, D.; Steinfeld, A. Carbon Dioxide Reforming of Methane Using an Isothermal Redox Membrane Reactor. *Energy Technology* **2015**, *3* (7), 784–789. https://doi.org/10.1002/ente.201500065.
- (27) Wang, I.; Gao, Y.; Wang, X.; Cai, R.; Chung, C.; Iftikhar, S.; Wang, W.; Li, F. Liquid Metal Shell as an Effective Iron Oxide Modifier for Redox-Based Hydrogen Production at Intermediate Temperatures. *ACS Catal.* **2021**, *11* (16), 10228–10238. https://doi.org/10.1021/acscatal.1c02102.
- (28) Wang, X.; Gao, Y.; Krzystowczyk, E.; Iftikhar, S.; Dou, J.; Cai, R.; Wang, H.; Ruan, C.; Ye, S.; Li, F. High-Throughput Oxygen Chemical Potential Engineering of Perovskite Oxides for Chemical Looping Applications. *Energy Environ. Sci.* **2022**, *15* (4), 1512–1528. https://doi.org/10.1039/D1EE02889H.

- (29) More, A.; Bhavsar, S.; Veser, G. Iron–Nickel Alloys for Carbon Dioxide Activation by Chemical Looping Dry Reforming of Methane. *Energy Technol.* **2016**, *4* (10), 1147–1157. https://doi.org/10.1002/ente.201500539.
- (30) Deml, A. M.; Stevanović, V.; Holder, A. M.; Sanders, M.; O'Hayre, R.; Musgrave, C. B. Tunable Oxygen Vacancy Formation Energetics in the Complex Perovskite Oxide Sr  $_x$  La  $_{1-x}$  Mn  $_y$  Al  $_{1-y}$  O  $_3$ . Chem. Mater. **2014**, 26 (22), 6595–6602. https://doi.org/10.1021/cm5033755.
- (31) Li, D.; Xu, R.; Gu, Z.; Zhu, X.; Qing, S.; Li, K. Chemical-Looping Conversion of Methane: A Review. *Energy Technol.* **2020**, *8* (8), 1900925. https://doi.org/10.1002/ente.201900925.
- (32) Zhu, X.; Li, K.; Neal, L.; Li, F. Perovskites as Geo-Inspired Oxygen Storage Materials for Chemical Looping and Three-Way Catalysis: A Perspective. *ACS Catal.* **2018**, *8* (9), 8213–8236. https://doi.org/10.1021/acscatal.8b01973.
- (33) More, A.; Hansen, C. J.; Veser, G. Production of Inherently Separated Syngas Streams via Chemical Looping Methane Cracking. *Catalysis Today* **2017**, *298*, 21–32. https://doi.org/10.1016/j.cattod.2017.07.008.
- (34) Kang, Y.; Han, Y.; Wei, C.; Liu, K.; Tian, M.; Huang, C.; Wang, C.; Lin, J.; Hou, B.; Pan, X.; Su, Y.; Li, L.; Zhang, R.; Hao, Y.; Wang, X. A Novel Carbon Cycle Process Assisted by Ni/La2O3 Catalyst for Enhanced Thermochemical CO2 Splitting. *Journal of Energy Chemistry* **2021**, *61*, 297–303. https://doi.org/10.1016/j.jechem.2021.03.026.
- (35) Fan, Z.; Weng, W.; Zhou, J.; Gu, D.; Xiao, W. Catalytic Decomposition of Methane to Produce Hydrogen: A Review. *Journal of Energy Chemistry* **2021**, *58*, 415–430. https://doi.org/10.1016/j.jechem.2020.10.049.
- (36) Gutta, N.; Velisoju, V. K.; Tardio, J.; Patel, J.; Satyanarayana, L.; Sarma, A. V. S.; Akula, V. CH 4 Cracking over the Cu–Ni/Al-MCM-41 Catalyst for the Simultaneous Production of H<sub>2</sub> and Highly Ordered Graphitic Carbon Nanofibers. *Energy Fuels* **2019**, *33* (12), 12656–12665. https://doi.org/10.1021/acs.energyfuels.9b02819.
- (37) Upham, D. C.; Agarwal, V.; Khechfe, A.; Snodgrass, Z. R.; Gordon, M. J.; Metiu, H.; McFarland, E. W. Catalytic Molten Metals for the Direct Conversion of Methane to Hydrogen and Separable Carbon. *Science* **2017**, *358* (6365), 917–921. https://doi.org/10.1126/science.aao5023.
- (38) Pudukudy, M.; Yaakob, Z.; Mazuki, M. Z.; Takriff, M. S.; Jahaya, S. S. One-Pot Sol-Gel Synthesis of MgO Nanoparticles Supported Nickel and Iron Catalysts for Undiluted Methane Decomposition into COx Free Hydrogen and Nanocarbon. *Applied Catalysis B: Environmental* **2017**, *218*, 298–316. https://doi.org/10.1016/j.apcatb.2017.04.070.
- (39) Sikander, U.; Samsudin, M. F.; Sufian, S.; KuShaari, K.; Kait, C. F.; Naqvi, S. R.; Chen, W.-H. Tailored Hydrotalcite-Based Mg-Ni-Al Catalyst for Hydrogen Production via Methane Decomposition: Effect of Nickel Concentration and Spinel-like Structures. *International Journal*

- *of Hydrogen Energy* **2019**, *44* (28), 14424–14433. https://doi.org/10.1016/j.ijhydene.2018.10.224.
- (40) Muraza, O.; Galadima, A. A Review on Coke Management during Dry Reforming of Methane: Revisiting Coke Management in Dry Reforming of Methane. *Int. J. Energy Res.* **2015**, 39 (9), 1196–1216. https://doi.org/10.1002/er.3295.
- (41) Buasuk, N.; Saelee, T.; Rittiruam, M.; Phatanasri, S.; Praserthdam, S.; Praserthdam, P. Deactivating and Non-Deactivating Coking Found on Ni-Based Catalysts during Combined Steam-Dry Reforming of Methane. *Top Catal* **2021**, *64* (5–6), 357–370. https://doi.org/10.1007/s11244-021-01413-4.
- (42) Zhou, J.; Zhao, J.; Zhang, J.; Zhang, T.; Ye, M.; Liu, Z. Regeneration of Catalysts Deactivated by Coke Deposition: A Review. *Chinese Journal of Catalysis* **2020**, *41* (7), 1048–1061. https://doi.org/10.1016/S1872-2067(20)63552-5.
- (43) Keller, M.; Sharma, A. Reverse Boudouard Reforming Produces CO Directly Suitable for the Production of Methanol from CO2 and CH4. *Chemical Engineering Journal* **2022**, *431*, 134127. https://doi.org/10.1016/j.cej.2021.134127.
- (44) Kim, Y.; Lim, H. S.; Lee, M.; Lee, J. W. Ni-Fe-Al Mixed Oxide for Combined Dry Reforming and Decomposition of Methane with CO2 Utilization. *Catalysis Today* **2021**, *368*, 86–95. https://doi.org/10.1016/j.cattod.2020.02.030.
- (45) Liao, X.; Long, Y.; Chen, Y.; Zangiabadi, A.; Wang, H.; Liu, Q.; Li, K.; Chen, X. Self-Generated Ni Nanoparticles/LaFeO3 Heterogeneous Oxygen Carrier for Robust CO2 Utilization under a Cyclic Redox Scheme. *Nano Energy* **2021**, *89*, 106379. https://doi.org/10.1016/j.nanoen.2021.106379.
- (46) Song, X.; Dong, X.; Yin, S.; Wang, M.; Li, M.; Wang, H. Effects of Fe Partial Substitution of La 2 NiO 4 /LaNiO 3 Catalyst Precursors Prepared by Wet Impregnation Method for the Dry Reforming of Methane. *Applied Catalysis A: General* **2016**, *526*, 132–138. https://doi.org/10.1016/j.apcata.2016.07.024.
- (47) Yang, E.; Noh, Y.; Ramesh, S.; Lim, S. S.; Moon, D. J. The Effect of Promoters in La 0.9 M 0.1 Ni 0.5 Fe 0.5 O 3 (M = Sr, Ca) Perovskite Catalysts on Dry Reforming of Methane. *Fuel Processing Technology* **2015**, *134*, 404–413. https://doi.org/10.1016/j.fuproc.2015.02.023.
- (48) Wang, H.; Dong, X.; Zhao, T.; Yu, H.; Li, M. Dry Reforming of Methane over Bimetallic Ni-Co Catalyst Prepared from La(CoxNi1-x)0.5Fe0.5O3 Perovskite Precursor: Catalytic Activity and Coking Resistance. *Applied Catalysis B: Environmental* **2019**, *245*, 302–313. https://doi.org/10.1016/j.apcatb.2018.12.072.
- (49) Hiremath, V.; Jadhav, A. H.; Lee, H.; Kwon, S.; Seo, J. G. Highly Reversible CO2 Capture Using Amino Acid Functionalized Ionic Liquids Immobilized on Mesoporous Silica. *Chemical Engineering Journal* **2016**, *287*, 602–617. https://doi.org/10.1016/j.cej.2015.11.075.

- (50) Switzer, J. R.; Ethier, A. L.; Flack, K. M.; Biddinger, E. J.; Gelbaum, L.; Pollet, P.; Eckert, C. A.; Liotta, C. L. Reversible Ionic Liquid Stabilized Carbamic Acids: A Pathway Toward Enhanced CO <sub>2</sub> Capture. *Ind. Eng. Chem. Res.* **2013**, *52* (36), 13159–13163. https://doi.org/10.1021/ie4018836.
- (51) Zhu, X.; Li, S.; Shi, Y.; Cai, N. Recent Advances in Elevated-Temperature Pressure Swing Adsorption for Carbon Capture and Hydrogen Production. *Progress in Energy and Combustion Science* **2019**, *75*, 100784. https://doi.org/10.1016/j.pecs.2019.100784.
- (52) Bukhtiyarova, M.; Lunkenbein, T.; Kähler, K.; Schlögl, R. Methanol Synthesis from Industrial CO2 Sources: A Contribution to Chemical Energy Conversion. *Catal Lett* **2017**, *147* (2), 416–427. https://doi.org/10.1007/s10562-016-1960-x.
- (53) Batiot-Dupeyrat, C.; Valderrama, G.; Meneses, A.; Martinez, F.; Barrault, J.; Tatibouët, J. M. Pulse Study of CO2 Reforming of Methane over LaNiO3. *Applied Catalysis A: General* **2003**, *248* (1–2), 143–151. https://doi.org/10.1016/S0926-860X(03)00155-8.
- (54) Mishra, A.; Dudek, R.; Gaffney, A.; Ding, D.; Li, F. Spinel Oxides as Coke-Resistant Supports for NiO-Based Oxygen Carriers in Chemical Looping Combustion of Methane. *Catalysis Today* **2019**, S092058611930505X. https://doi.org/10.1016/j.cattod.2019.09.010.
- (55) Das, S.; Bhattar, S.; Liu, L.; Wang, Z.; Xi, S.; Spivey, J. J.; Kawi, S. Effect of Partial Fe Substitution in La <sub>0.9</sub> Sr <sub>0.1</sub> NiO <sub>3</sub> Perovskite-Derived Catalysts on the Reaction Mechanism of Methane Dry Reforming. *ACS Catal.* **2020**, *10* (21), 12466–12486. https://doi.org/10.1021/acscatal.0c01229.
- (56) Faroldi, B. M.; Múnera, J. F.; Cornaglia, L. M. In Situ Characterization of Phase Transformation and Reactivity of High Surface Area Lanthanum-Based Ru Catalysts for the Combined Reforming of Methane. *Applied Catalysis B: Environmental* **2014**, *150–151*, 126–137. https://doi.org/10.1016/j.apcatb.2013.12.005.
- (57) Mishra, A.; Li, F. Chemical Looping at the Nanoscale Challenges and Opportunities. *Current Opinion in Chemical Engineering* **2018**, *20*, 143–150. https://doi.org/10.1016/j.coche.2018.05.001.
- (58) Zeng, L.; Cheng, Z.; Fan, J. A.; Fan, L.-S.; Gong, J. Metal Oxide Redox Chemistry for Chemical Looping Processes. *Nat Rev Chem* **2018**, *2* (11), 349–364. https://doi.org/10.1038/s41570-018-0046-2.
- (59) Cho, P.; Mattisson, T.; Lyngfelt, A. Defluidization Conditions for a Fluidized Bed of Iron Oxide-, Nickel Oxide-, and Manganese Oxide-Containing Oxygen Carriers for Chemical-Looping Combustion. *Ind. Eng. Chem. Res.* **2006**, *45* (3), 968–977. https://doi.org/10.1021/ie050484d.
- (60) Purnomo, V.; Yilmaz, D.; Leion, H.; Mattisson, T. Study of Defluidization of Iron- and Manganese-Based Oxygen Carriers under Highly Reducing Conditions in a Lab-Scale Fluidized-Bed Batch Reactor. *Fuel Processing Technology* **2021**, *219*, 106874. https://doi.org/10.1016/j.fuproc.2021.106874.

- (61) Liu, L.; Kong, B.; Jiao, Q.; Yang, J.; Liu, Q.; Liu, X. Structure Characterization and CO <sub>2</sub> Gasification Kinetics of Tri-High Coal-Chars Derived from High-Temperature Pyrolysis. *ACS Omega* **2019**, *4* (21), 19030–19036. https://doi.org/10.1021/acsomega.9b02024.
- (62) He, L.; Liao, G.; Li, H.; Ren, Q.; Hu, S.; Han, H.; Xu, J.; Jiang, L.; Su, S.; Wang, Y.; Xiang, J. Evolution Characteristics of Different Types of Coke Deposition during Catalytic Removal of Biomass Tar. *Journal of the Energy Institute* **2020**, *93* (6), 2497–2504. https://doi.org/10.1016/j.joei.2020.08.009.
- (63) Ferrari, A. C.; Robertson, J. Raman Spectroscopy of Amorphous, Nanostructured, Diamond–like Carbon, and Nanodiamond. *Philosophical Transactions of the Royal Society of London. Series A: Mathematical, Physical and Engineering Sciences* **2004**, *362* (1824), 2477–2512. https://doi.org/10.1098/rsta.2004.1452.
- (64) Cançado, L. G.; Takai, K.; Enoki, T.; Endo, M.; Kim, Y. A.; Mizusaki, H.; Jorio, A.; Coelho, L. N.; Magalhães-Paniago, R.; Pimenta, M. A. General Equation for the Determination of the Crystallite Size La of Nanographite by Raman Spectroscopy. *Appl. Phys. Lett.* **2006**, *88* (16), 163106. https://doi.org/10.1063/1.2196057.
- (65) Wu, Z.; Stair, P. UV Raman Spectroscopic Studies of V/θ-Al2O3 Catalysts in Butane Dehydrogenation. *Journal of Catalysis* **2006**, *237* (2), 220–229. https://doi.org/10.1016/j.jcat.2005.11.005.